Double-Zero-Index Structural Phononic Waveguides

Hongfei Zhu[1,2,*] and Fabio Semperlotti[2,†]
[1]*Department of Aerospace and Mechanical Engineering, University of Notre Dame,*
Notre Dame, Indiana 46556, USA
[2]*Ray W. Herrick Laboratories, School of Mechanical Engineering,*
Purdue University, West Lafayette, Indiana 47907, USA

(Received 21 July 2017; revised manuscript received 21 October 2017; published 29 December 2017)

We report on the theoretical and experimental realization of a double-zero-index elastic waveguide and the corresponding acoustic cloaking and supercoupling effects. The proposed waveguide uses geometric tapers in order to induce Dirac-like cones at $\vec{k} = 0$ due to accidental degeneracy. The nature of the degeneracy is explored by a $k \cdot p$ perturbation method adapted to thin structural waveguides. The results confirm the linear nature of the dispersion around the degeneracy and the possibility to map the material to effective-medium properties. Effective parameters numerically extracted using boundary medium theory confirm that the phononic waveguide maps into a double-zero-index material. Numerical and experimental results confirm the expected cloaking and supercoupling effects.

DOI: 10.1103/PhysRevApplied.8.064031

I. INTRODUCTION

The concept of acoustic metamaterials [1,2] has rapidly emerged as a powerful alternative to design materials and structures exhibiting unexpected dynamic properties typically not achievable in natural materials. The early development of the concept of metamaterials dates back to 1968 when Veselago [3] predicted materials exhibiting simultaneously negative permeability and permittivity. Such negative index media remained substantially unexploited until, almost 30 yr later, Pendry [4] suggested the possibility to achieve the amplification of evanescent waves, which would have profound effects on lens design and imaging applications. Experimental observation of negative index materials was provided shortly afterward by Smith [5,6], who designed a periodic array of interspaced conducting and nonmagnetic split-ring resonators. Following these studies, the scientific community has rapidly extended the underlying physical concepts to other fields of classical mechanics such as acoustics and elastodynamics. In less than two decades, this concept has allowed a drastic expansion of the material design space enabling applications involving acoustic wave management and control. Properties such as acoustic band gaps [7–12], focusing [13–17], collimation [18–20], subwavelength resolution [21–26], and negative refraction [27–30] have been discovered and studied in depth. More recently, researchers have shown a rather exciting property of these materials consisting of their ability to achieve near-zero effective parameters. This class of materials was formulated for electromagnetic waves where epsilon-near-zero (ENZ), mu-near-zero, and epsilon-and-mu-near-zero (EMNZ) properties were obtained. Applications included antenna designs with high directivity [31,32] and enhanced radiation efficiency [33,34], as well as the realization of unconventional tunneling of electromagnetic energy within ultrathin subwavelength channels or bends [35–37]. Among the most peculiar characteristics of these materials, we mention the independence of the phase from the propagation distance. This means that a wave entering a double-zero-index material emerges on the other side having the exact same phase as the input. In addition, double-zero materials are also characterized by a high level of transmissibility, ideally acting as a nonreflective waveguide even in the presence of sharp impedance discontinuities.

In analogy with an EMNZ, an acoustic double-zero-index material (DZIM) corresponds to a medium with simultaneous zero effective mass density and elastic compliance. While materials with near-zero permittivity are available in nature (e.g., some noble metals, doped semiconductors [38], polar dielectrics [39], and transparent conducting oxide [40]), in acoustics, near-zero density and elastic compliance must be achieved via effective quantities by leveraging the local dynamic response of the medium. In the past few years, some acoustic metamaterials were reported to exhibit single zero effective parameters, such as near-zero density [41–43]. We note that this behavior is the exact counterpart of single zero electromagnetic materials, such as the ENZ. Although these materials offered good control on the phase, they suffered from low transmissibility due to an intrinsic impedance mismatch between the host and the zero effective density medium. Double-zero materials target specifically this limitation of the transmission properties. However, designing acoustic media with double-zero effective properties is not a trivial task given that they are not readily available in nature.

---

[*] Hongfei.Zhu.44@nd.edu
[†] Corresponding author.
fsemperl@purdue.edu

Recent studies of photonic and phononic crystals [44–50] revealed that when a Dirac-like cone (DC) can be obtained at the center of the Brillouin zone, such a lattice can be mapped into a double-zero refractive-index material. This observation has drastically extended the possibility to design materials having near-zero effective properties. Nevertheless, while different applications of this basic concept were explored in photonics and phononics, there has been very little research targeting the implementation of these effective material properties in solids [44,51]. The research on elastic phononic waveguides has been lagging behind even more, and it currently counts no attempt of designing zero-index properties. In addition, the experimental implementation and validation of zero-index elastic media has not been reported in the scientific literature, mostly due to the complexities associated with their design and fabrication.

In the present study, we report on the theoretical, numerical, and experimental realization of a structural phononic waveguide exhibiting double-zero-index behavior and capable of achieving acoustic cloaking and supercoupling. The proposed design builds upon a class of metamaterials recently introduced by the authors [52–54] and based on geometric tapers realized in a single-material system. The specific design employed in this study can be thought of as an equivalent locally resonant unit where an internal resonating core is embedded within a more compliant medium (i.e., the taper). Geometrically tapered metamaterials [52] exhibit DCs at the center of the Brillouin zone (Γ point) that are the result of accidental degeneracies [55]. In other terms, the degeneracy is induced by the specific combination of the geometric parameters of the tapers, and it is not protected by the underlying lattice structure (like, for example, in graphene). The bands emanating from the threefold degenerate point (the Dirac-like point) exhibit isotropic linear dispersion. We show that these properties are the foundation that allows us to achieve double-zero effective properties in this class of materials. In particular, we show that in the neighborhood of this degenerate point, our waveguide exhibits simultaneous zero mass density and zero reciprocal shear modulus (or, equivalently, infinite shear modulus or zero elastic compliance in shear).

Possible applications of such materials may include, but are not limited to, efficient energy transmission across discontinuities (e.g., joints in thin-walled structures) and the consequent reduction of localization effects and dynamic amplification, efficient energy extraction for dissipation and/or harvesting, regardless of the location or the spatial distribution of the acoustic source, and vibration isolation of sensitive components. We anticipate the proposed DZIM design to be virtually scalable to any frequency range and geometric dimensions. In the case of lightweight structural applications, such as those involved in many transportation systems, the typical dimensions of the unit cell will range between 2 and 6 mm in thickness and 1 to 4 cm in terms of lattice constant. Such dimensions will allow elastic wave control via DZIM properties in a frequency range of approximately 20 to 100 kHz (considering aluminum alloys). Equivalently, the wavelength will range between 6 and 1.5 cm. In more general terms, a straightforward approach to rescale the proposed design in order to operate at different frequencies consists of isotropically rescaling the dimensions and the dispersion properties by keeping $\lambda/L = \mathrm{const}$, where L is the lattice constant, and λ is the wavelength at a frequency f. As an example, dividing all the geometric dimensions by a factor of 2 will double the operating frequency. This approach will allow a simple rescaling without requiring a complete redesign of the unit. It is foreseeable that the DZIM design can be implemented also at microscales. Many applications in the telecommunications area exploit analog filtering of surface acoustic waves as an integral part of their modulation or demodulation systems. DZIM-based filters can open possibilities to carefully tailor the transfer function of these systems. The rescaling argument discussed above suggests that at submillimiter scales, the design will experience a substantial increase in the operating frequencies that will likely belong to the low-megahertz range while transitioning to the high-megahertz range for dimensions on the order of microns. From a fabrication perspective, it is expected that the currently available additive manufacturing techniques already allow sufficient precision to build such materials.

II. RESULTS

A. Double-zero-index waveguide via geometric tailoring

The proposed phononic waveguide employs a tapered unit cell in a square lattice configuration (C_{4v} symmetry). The unit cell consists of a square plate having an embedded elliptic toruslike taper and a (resonating) center mass. The unit is also symmetric with respect to the midplane of the waveguide (Fig. 1). The x-z cross section of the unit is shown in Fig. 1(b) and shows the main geometric parameters where t is the thickness of the element, L is the lattice constant, a and b are the lengths of the minor and major axes of the ellipse, r is the radius of the torus, and h is the thickness of the center mass. The unit is made out of aluminum with mass density $\rho = 2700\ \mathrm{kg/m^3}$, Young's modulus $E = 70$ GPa, and Poisson's ratio $\nu = 0.33$.

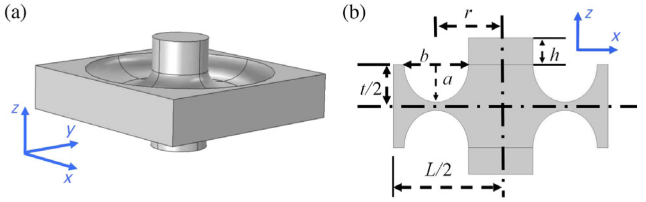

FIG. 1. Schematic of (a) the fundamental tapered unit cell and (b) its x-z cross section showing the main geometric parameters. The tapered geometry is symmetric with respect to the midplane of the plate.

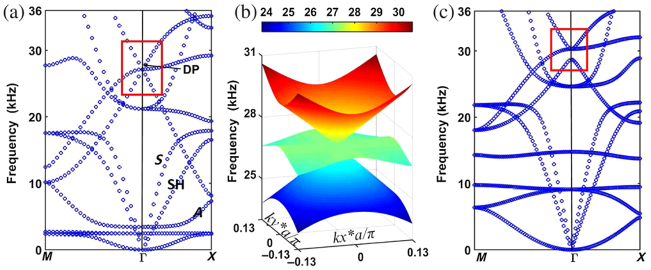

FIG. 2. (a) The dispersion relations around $f = 27.02$ kHz showing the existence of a triple-degenerate point and a Dirac-like cone (red box) for a given selection of the taper parameters. (b) Equifrequency-surface plot corresponding to the frequency range around the DP and showing the formation of the Dirac-like cones. (c) When the geometric configuration is slightly perturbed (taper coefficient a changes from 0.0039 to 0.0035) the Dirac-like cone opens up, confirming that the formation of the linear dispersions is due to an accidental degeneracy.

The dispersion relations for the proposed system are calculated using a commercial finite-element solver (COMSOL MULTIPHYSICS). Given the finite dimension of the unit cell in the thickness direction, the dispersion curves are composed by symmetric (S), antisymmetric (A), and shear horizontal (SH) guided Lamb modes. By using a proper selection of the geometric parameters (specifically, $L = 0.04$ m, $t = 0.008$ m, $a = 0.0039$ m, $b = 0.007442$ m, $r = 0.012$ m, and $h = 0.013$ m), the band structure of the waveguide is tuned to exhibit a threefold degenerate point (the Dirac-like point, DP) at $f = 27.04$ kHz and $\vec{k} = 0$ [Fig. 2(a)]. Note that the branches emanating from the degenerate point are isotropic and linear and form two cones touching their vertices at the DP [Fig. 2(b)]. The cones are made of A_0 modes having nonzero but constant group velocity and are intersected by an A_0 flatband at the DP.

The Dirac-like cone is the result of an accidental degeneracy, which can be confirmed by slightly perturbing the geometric parameters. By perturbing the toruslike taper a (from 0.0039 to 0.0035) the cones separate [Fig. 2(c)] and the triple-degenerate point splits into a nondegenerate and a doubly degenerate band. The corresponding eigenstates of the three degenerate modes are provided in Fig. 4(a), which shows, from top to bottom, the lower cone, the flatband, and the upper cone.

B. Analysis of the Dirac-like cones

To further understand the origin of the Dirac-like dispersion, we extend the $\vec{k} \cdot \vec{p}$ method (well known in electronic applications [56]) to analyze our phononic system. This method was recently adopted by Mei *et al.* [55] to analyze the Dirac and Dirac-like cones in two-dimensional phononic (sonic) and photonic crystals.

Our system is described by Navier's equations with traction-free boundary conditions on the top and bottom surfaces of the waveguide. Imposing such boundary conditions when in the presence of tapers creates nontrivial complexities due to the changing direction of the unit vector normal to the tapered surface. To simplify the modeling, we resort to an approach previously used to extend the three-dimensional plane-wave expansion method to 2D phononic waveguides [52,57]. According to this method, we can view the two-dimensional waveguide as part of a three-dimensional, layered, periodic bulk material constructed by alternating the waveguide with vacuum layers [Fig. 3(a)] along the thickness direction. The vacuum layers have negligible mass density and modulus to allow for the traction-free boundary conditions on the surface of the waveguide to be automatically satisfied. The three-dimensional periodic medium so obtained, whose unit cell is shown in Fig. 3(b), can be modeled as a layered bulk material by Navier's equations and solved in order to extract the dispersion relations. Note that the use of the vacuum layer ensures that the periodic images of the waveguide along the thickness direction are dynamically decoupled from each other, therefore, simply resulting in repeated roots in the dispersion calculation. This approach allows an efficient implementation of the adapted $\vec{k} \cdot \vec{p}$ method for bulk elastic systems as we present below.

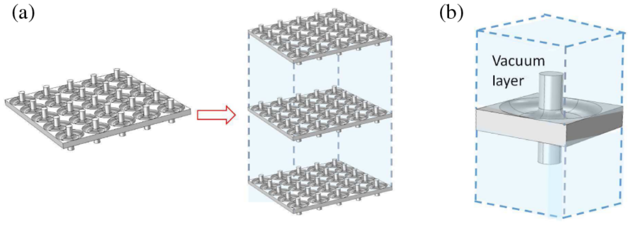

FIG. 3. Schematics of (a) the periodic waveguide and its assembly in a 3D bulk layered medium used to calculate the dispersion relations. (b) Detailed view of the unit cell of the 3D bulk periodic medium showing the waveguide unit cell and the vacuum layers.

We can then write the general form of Navier's equations for an inhomogeneous bulk medium in the vector form as

$$-\rho\omega^2\vec{U} = (\lambda + \mu)\mathbf{\nabla}(\mathbf{\nabla} \cdot \vec{U}) + \mu\mathbf{\nabla}^2\vec{U} + \mathbf{\nabla}\lambda\mathbf{\nabla} \cdot \vec{U} + \mathbf{\nabla}\mu \times \mathbf{\nabla} \times \vec{U} + 2(\mathbf{\nabla}\mu \cdot \mathbf{\nabla})\vec{U}. \tag{1}$$

Here, $\vec{U}(\vec{r})$ is the particle displacement vector, $\rho(\vec{r})$ is the local density, and $\lambda(\vec{r})$ and $\mu(\vec{r})$ are the local Lamé constants, which are all functions of the spatial variables.

According to Mei *et al.* [55], we assume that all the Bloch states at the Γ point ($\vec{k}_0 = 0$) are known and given by $\vec{U}_{n0}(\vec{r}) = e^{i\vec{k}_0 \cdot \vec{r}}\vec{\psi}_{n0}(\vec{r}) = \vec{\psi}_{n0}(\vec{r})$, as well as the corresponding eigenfrequency ω_{n0}, where "n" denotes the band index. The Bloch states at a generic wave vector $\vec{k}$ near $\vec{k}_0 = 0$ can then be written as

$$\begin{aligned}\vec{U}_{n\vec{k}}(\vec{r}) &= \vec{\psi}_{n\vec{k}}(\vec{r})e^{i\vec{k}\cdot\vec{r}} = e^{i\vec{k}\cdot\vec{r}}\sum_j A_{nj}(\vec{k})\vec{\psi}_{j0}(\vec{r})\\ &= \sum_j A_{nj}(\vec{k})e^{i(\vec{k}-\vec{k}_0)\cdot\vec{r}}\vec{U}_{j0}(\vec{r})\\ &= \sum_j A_{nj}(\vec{k})e^{i\vec{k}\cdot\vec{r}}\vec{U}_{j0}(\vec{r}), \qquad (2)\end{aligned}$$

where the unknown periodic functions $\vec{\psi}_{n\vec{k}}(\vec{r})$ are expressed as a linear combination of the $\vec{\psi}_{j0}(\vec{r})$. Substituting Eq. (2) into Eq. (1) and collecting terms linear in $\vec{k}$, we obtain

$$\begin{aligned}&\sum_j A_{nj}(\vec{k})e^{i\vec{k}\cdot\vec{r}} \times \{\rho(\vec{r})(\omega_{n\vec{k}}^2 - \omega_{j0}^2)\vec{U}_{j0}(\vec{r})\\ &\quad + 2\mu(\vec{r})i\vec{k}\cdot[\nabla\vec{U}_{j0}(\vec{r})] + (\lambda(\vec{r}) + \mu(\vec{r}))\nabla[i\vec{k}\cdot\vec{U}_{j0}(\vec{r})]\\ &\quad + (\lambda(\vec{r}) + \mu(\vec{r}))i\vec{k}[\nabla\cdot\vec{U}_{j0}(\vec{r})]\\ &\quad + \nabla\lambda(\vec{r})[i\vec{k}\cdot\vec{U}_{j0}(\vec{r})] + \nabla\mu(\vec{r})\times[i\vec{k}\times\vec{U}_{j0}(\vec{r})]\\ &\quad + 2[\nabla\mu\cdot i\vec{k}]\vec{U}_{j0}(\vec{r}) + o(k^2)\} = 0. \qquad (3)\end{aligned}$$

Utilizing the orthonormality property of the basis functions $\vec{U}_{j0}(\vec{r})$, i.e., $[(2\pi)^3/V]\int_{\text{unit cell}}\rho(\vec{r})\vec{U}_{j0}(\vec{r})\cdot\vec{U}_{l0}^*(\vec{r})d\vec{r} = \delta_{jl}$, where V is the volume of the unit cell, Eq. (3) can be written as

$$\sum_j[(\omega_{n\vec{k}}^2 - \omega_{j0}^2)\delta_{lj} + P_{jl}(\vec{k})]A_{nj}(\vec{k}) = 0, \qquad (4)$$

where

$$P_{jl}(\vec{k}) = i\vec{k}\cdot\vec{p}_{jl}(\vec{k}), \qquad (5)$$

and up to the first order in $\vec{k}$, we can write

$$\begin{aligned}p_{jl}(\vec{k}) = \frac{(2\pi)^3}{V}\int_{\text{unit cell}}&\{(\lambda+\mu)(\nabla\vec{U}_{j0})^T\cdot\vec{U}_{l0}^*\\ &+ (\lambda+\mu)[\nabla\cdot\vec{U}_{j0}(\vec{r})]\vec{U}_{l0}^* + 2\mu\nabla\vec{U}_{j0}\cdot\vec{U}_{l0}^*\\ &+ [\nabla\lambda\cdot\vec{U}_{l0}^*]\vec{U}_{j0} + 2(\vec{U}_{j0}\cdot\vec{U}_{l0}^*)\nabla\mu\\ &+ [\nabla\mu\cdot\vec{U}_{j0}]\vec{U}_{l0}^* - [\vec{U}_{j0}\cdot\vec{U}_{l0}^*]\nabla\mu\}. \qquad (6)\end{aligned}$$

Equation (4) has nontrivial solutions only when the following secular equation is satisfied,

$$\det|(\omega_{n\vec{k}}^2 - \omega_{j0}^2)I + P(\vec{k})| = 0, \qquad (7)$$

where I is the identity matrix. Since we are interested in the linear dispersions of the Dirac-like cone, we consider only the degenerate states at the Dirac-like point in the summation of Eq. (2). In fact, other bands contribute only to the higher-order terms of $\vec{k}$. For small $\vec{k}$, the analytic solution for Eq. (7) can be expressed as

$$\frac{-2\omega_{j0}\Delta\omega}{\Delta k} = \gamma_\beta + o(\Delta k), \qquad \beta = 1, 2, 3, \qquad (8)$$

where we approximate the term $\omega_{j0}^2 - \omega_{n\vec{k}}^2$ as $-2\omega_{j0}(\Delta\omega)$.

After evaluating Eq. (6) numerically (detailed expressions of its elements can be found in the Appendix), the reduced Hamiltonian matrix for our system is given by

$$\vec{p}_{jl} = 10^8\begin{pmatrix}(0,0) & (0.002, -4.9983) & (-4.9902, -0.002)\\ (-0.002, 4.9930) & (0,0) & (0,0)\\ (4.9849, 0.002) & (0,0) & (0,0)\end{pmatrix}. \qquad (9)$$

Note that $\vec{p}_{12} = -\vec{p}_{21}$, $\vec{p}_{13} = -\vec{p}_{31}$, $|p_{12}| = |p_{13}|$, and $\vec{p}_{12}\perp\vec{p}_{13}$; these properties are required to guarantee the isotropy of the cones. By substituting Eq. (9) into Eq. (7), we get the dispersion relations of the modes contributing to the Dirac-like cone,

$$\begin{aligned}&\frac{\Delta f}{\Delta k} = 0,\\ &\frac{\Delta f}{\Delta k} = \pm\frac{|\vec{p}_{12}|}{8\pi^2 f_0} = \pm 233.48. \qquad (10)\end{aligned}$$

Obviously, the first result in Eq. (10) corresponds to the flatband, while the remaining two signed values correspond to the linear dispersion associated with the cones. Note that these results do not depend on the wave-vector $\vec{k}$ direction, thus, confirming the isotropy of the linear dispersion. Equation (10) can be plotted together with the numerically obtained dispersion relations [Fig. 4(b)] in order to illustrate the good agreement between the $\vec{k}\cdot\vec{p}$ method and the full-field numerical results. It can be seen from Eq. (6) that the linear slopes γ_β are determined only by the nondiagonal element of the p_{jl} matrix. This term represents the strength of the coupling between the degenerate states and indicates that the frequency repulsion effect gives rise to the Dirac-like cones.

C. Effective-medium properties

Under certain conditions, the characteristics of the medium around the Dirac-like point can be mapped to effective-medium properties. This manipulation allows a very clear characterization of the double-zero properties.

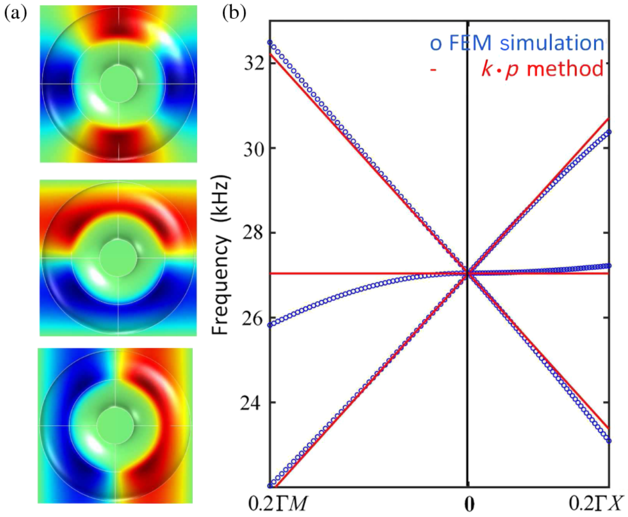

FIG. 4. (a) The eigenstates corresponding to the three degenerate states at the DP. From top to bottom, we find the state of the negative slope band, the flatband, and the positive band. (b) Comparison of the linear dispersion prediction at the DP obtained from the $\vec{k}\cdot\vec{p}$ method and the finite-element simulations.

Note that although the selected DP has a relatively high frequency (the wavelength in an equivalent flat plate is about $1.25L$), we employ the boundary effective-medium theory [58] to obtain the equivalent effective material parameters. It has been argued [59,60] that for periodic media, the effective-medium theory [61,62] is still valid at $\vec{k}=\vec{0}$ around the standing wave frequency even when, strictly speaking, the frequency belongs to the short-wavelength regime. From a more empirical perspective, we also show that the use of the effective-medium description matches well the finite-element-model predictions, therefore, further confirming the validity of the effective-medium approach.

The boundary effective-medium theory [58] treats the unit cell as a *black box* that responds to an incoming wave. According to this method, we calculate the eigenstates and then evaluate the modal effective forces, displacements, strains, and stresses from the response collected along the boundaries of the unit cell. The effective density and modulus are then extracted by using Newton's second law and the constitutive relations.

As an example, for the eigenstates along the ΓX direction, the effective mass density can be obtained from Newton's second law as

$$\rho^{\mathrm{eff}}=\frac{m^{\mathrm{eff}}}{L^2h}=\frac{F_z^{\mathrm{eff}}}{\ddot{u}_z^{\mathrm{eff}}L^2h}=\frac{-F_z^{\mathrm{eff}}}{\omega^2u_z^{\mathrm{eff}}L^2h},\qquad(11)$$

where ρ^{eff} is the effective mass density, F_z^{eff} is the effective net force exerted on the unit cell in the out-of-plane Z direction, and u_z^{eff} is the effective displacement of the unit cell in the z direction resulting from the three degenerate states contributing to the Dirac-like cone. F_z^{eff} and u_z^{eff} can be obtained as

$$\begin{aligned}F_z^{\mathrm{eff}}=&\int T_{xz}dydz\Big|_{x=L}-\int T_{xz}dydz\Big|_{x=0}\\&+\int T_{yz}dxdz\Big|_{y=L}-\int T_{yz}dxdz\Big|_{y=0}\end{aligned}\qquad(12)$$

and

$$u_z^{\mathrm{eff}}=\frac{\int u_zdydz|_{x=L}+\int u_zdydz|_{x=0}}{2Lh}.\qquad(13)$$

Since all the contributing modes are antisymmetric modes, we consider only the effective shear moduli. They can be obtained from the constitutive relations as follows:

$$\begin{aligned}T_{xz}^{\mathrm{eff}}&=G^{\mathrm{eff}}S_{xz},\\T_{yz}^{\mathrm{eff}}&=G^{\mathrm{eff}}S_{yz},\end{aligned}\qquad(14)$$

where G^{eff} is the effective shear modulus, and T^{eff} and S^{eff} are the effective stress and strain tensors. Using the first of Eq. (14) as an example, the stress and strain can be obtained as

$$T_{xz}^{\mathrm{eff}}=\frac{\int T_{xz}dydz|_{x=L}+\int T_{xz}dydz|_{x=0}}{2Lh}\qquad(15)$$

and

$$S_{xz}^{\mathrm{eff}}=\frac{\int u_zdydz|_{x=L}-\int u_zdydz|_{x=0}}{L^2h}.\qquad(16)$$

Figures 5(a) and 5(c) show the effective shear modulus and the effective mass density as functions of frequency in the range around the Dirac-like point. The results clearly indicate that below the DP, the proposed metamaterial design behaves as a double-negative material, while above

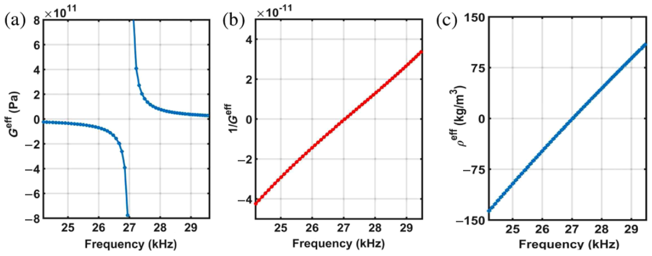

FIG. 5. Frequency dependence of (a) the effective shear modulus G^{eff}, (b) the reciprocal effective shear modulus $1/G^{\mathrm{eff}}$, and (c) the effective mass density ρ^{eff} near the Dirac-like point.

the DP, it behaves as a double-positive material. Similarly, the calculation of the reciprocal effective shear modulus [Fig. 5(b)] shows that both ρ^{eff} and $1/G^{\mathrm{eff}}$ vary linearly and become zero simultaneously as the frequency crosses the Dirac-like point. These results suggest that the proposed metamaterial should exhibit propagation properties consistent with a double-zero-index material. In particular, we expect that acoustic waves traveling through the medium at the DP frequency should not experience any spatial phase change.

D. Full-field numerical analyses

In order to validate the theoretical predictions, we build a numerical model of an elastic waveguide made out of the proposed double-zero-index material. The basic test structure consists of a flat plate with an 11×12 lattice of toruslike tapers embedded in the center [Figs. 6(a) and 6(b)]. Both the left and right boundaries are treated with perfectly matched layers (not shown) to avoid reflections, while the top and bottom boundaries are treated with periodic boundary conditions in order to simulate an infinite plate. The zero-index material slab is excited from the left by a planar A_0 wave at $f = 27.04$ kHz and normal incidence. The resulting wave field [Fig. 6(a)] indicates that no phase change occurs inside the metamaterial slab and nearly full transmission is achieved due to the zero refractive index and the matched impedance with the flat plate. These peculiar transmission properties are tested to show the ability to achieve cloaking and supercoupling in structural waveguides.

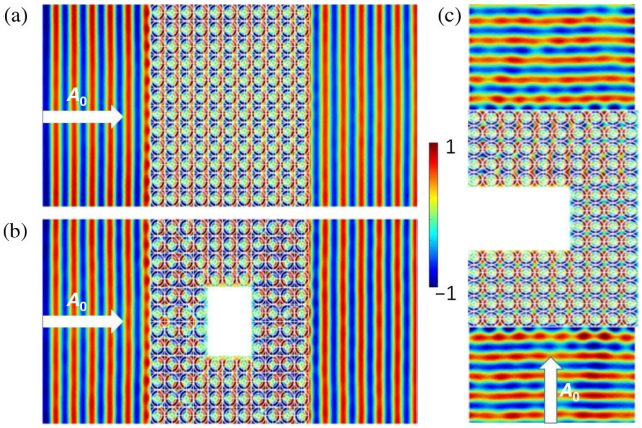

FIG. 6. (a) The out-of-plane displacement distribution of the wave field when an incident A_0 planar wave at $f = 27.04$ kHz impinges normally onto the 11×12 lattice of double-zero-index material. The top and bottom boundaries are treated with periodic boundary conditions, while the left and right boundaries use perfectly matched layers to avoid reflections. As expected, no phase change occurs inside the metamaterial slab. (b) The out-of-plane displacement field showing the cloaking capability of the double-zero material when an object 3×4 units in dimension is embedded in the slab. (c) The out-of-plane displacement field showing the supercoupling capabilities when a U-shaped narrow channel is filled with the double-zero material.

To illustrate the cloaking capability, we embed an object (represented by a through-hole opening 3×4 units in size) within the DZIM metamaterial. The opening has clamped boundary conditions. The remaining conditions are unchanged with respect to the case we discuss above. The numerical results [Fig. 6(b)] show that the wave emerges on the opposite side of the slab being completely unaffected. Comparing these results with Fig. 6(a), we see that the acoustic field downstream of the scatterer does not carry any information about the scatterer itself, therefore, confirming the cloaking capability of the medium.

In a similar way, we test the transmission performance of a U-shaped waveguide channel. The change in cross section is operated within the double-zero-index slab by shrinking the middle section from 10 to 4 units. Similar to the cloaking case, clamped boundary conditions are imposed on all the walls of the U-shaped waveguide, while the remaining boundaries are left free. In addition, perfectly matched layers are used on the top and bottom surfaces to absorb the outgoing waves and eliminate reflections. We observe that the incident plane wave (A_0 mode at $f = 27.04$ kHz) propagated through the U-shaped channel is completely unaffected, while picking up only a minor phase distortion. Considering the large extent of the impedance discontinuity induced within the DZIM slab, this distortion is almost negligible. Figure 10 in the Appendix provides the contour plots in terms of amplitude and phase corresponding to the results [Figs. 6(b) and 6(c)]. In conclusion, these results confirm the ability of the proposed design to create supercoupling effects in structural waveguides.

E. Experimental results

We perform an experimental investigation in order to validate the concept of a DZIM structural waveguide. We select the supercoupling case for testing because it is the most challenging condition to achieve and, therefore, the most representative of the actual performance. To facilitate fabrication and testing, we rescale the structure by reducing the plate thickness to 0.004 m and the unit cell dimension to half the original size. The rescaled design results in a Dirac-like point at 54.08 kHz. The test sample is fabricated with extended edges along the U-shaped waveguide channel in order to be able to enforce the boundary conditions. For simplicity, instead of creating a complex setup to impose the clamped conditions used in the simulation results [Fig. 6(c)], we decide to treat the edges of the U-section with a viscoelastic damping material while clamping the remaining edges.

The toruslike tapers are computer-numerical-control machined from an initially flat aluminum plate, while the center masses are cut from aluminum bars and successively glued on the taper. The experimental sample is mounted vertically in an aluminum frame, and viscoelastic tape is applied on the top and bottom edges in order to minimize reflections from the boundaries. An array of microfiber composite (MFC) patches [Fig. 7(a)] is surface bonded on the plate and simultaneously actuated to generate a quasi-A_0 planar incident wave. The out-of-plane response (velocity) of the entire plate is acquired using a Polytec PSV-500 laser-scanning vibrometer. We perform both steady-state and transient measurements. The steady-state response is collected following a harmonic excitation at the target frequency of 54.1 kHz. The time transient measurement is obtained in response to a 50-count wave-burst excitation signal having a 54.1-kHz center frequency. Figure 7(b) shows the measured out-of-plane velocity field at a fixed time instant, while the inset provides an enlarged view of the wave field in the area after the DZIM slab. The data in this inset are obtained from a separate time transient scan which is performed exclusively on the area following the DZIM [white dashed box in Fig. 7(a)] by using an increased scanning mesh size (for improved resolution) and a rescaled color bar range. Despite some unwanted reflections due to the finite size of the test sample, the planar nature of the transmitted wave field is clearly recognizable. At the same time, the transmitted intensity is subject to a substantial level of attenuation. Figures 7(c) and 7(d) show the amplitude and phase distribution of the steady-state response at the target frequency. Overall, the phase-field distribution over the entire structure [Fig. 7(d)] appears consistent with the numerical results (see Fig. 10 in the Appendix), and the planar nature of the transmitted wave fields is still well identifiable. Similarly, the amplitude field distribution [Fig. 7(c)] highlights the attenuation in the intensity as the wave is transmitted through the DZIM section.

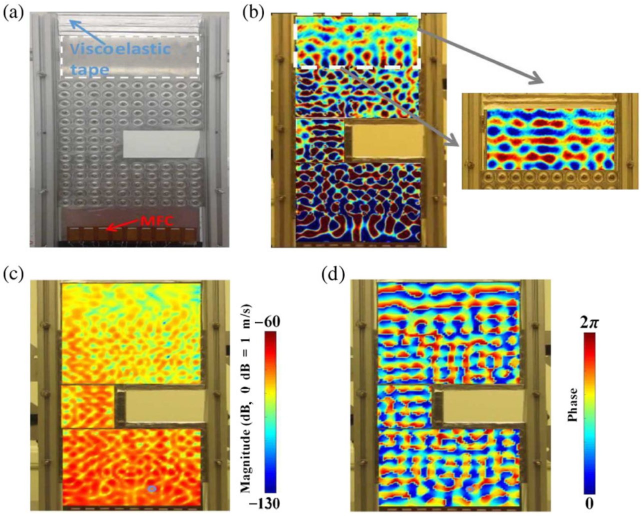

FIG. 7. Experimental setup and results. (a) Front view of the test bed consisting of a 4-mm-thick aluminum plate with a U-shaped waveguide channel filled with DZIM material. An array of MFC patches is surface bonded to generate the ultrasonic excitation. The scans cover the entire plate including the DZIM section where the out-of-plane velocity response is measured. (b) The measured transmitted A_0 wave field (out-of-plane velocity) showing that the waves propagate through the U-shaped channel preserving its planar nature. The inset shows an enlarged view of the wave field after the DZIM section (marked by the white dashed box). This data are obtained by performing a separate time transient scan that employs a refined scanning mesh grid and a rescaled color bar range. (c) and (d) show the amplitude and phase distribution of the steady-state responses of the whole structure at the targeted frequency.

To further understand the origin of the large attenuation of the transmitted amplitude, we perform additional numerical analysis by taking into account the effect of damping. Aluminum has a small intrinsic loss factor that can vary depending on the specific type of alloy and manufacturing treatments but that generally never exceeds $\eta_s = 0.01$. Hence, we add this loss factor to the whole structure by using a complex notation of Young's modulus $E = E_0(1 + \eta_s j)$. The amplitude and phase distribution of the wave field for the case of supercoupling are recalculated, and the results are provided in Figs. 8(a) and 8(b). These results are in much better agreement with the experimental observations, therefore, confirming the limited effect of damping on the phase distribution and the large impact on the amplitude attenuation. Given the large observed attenuation somewhat beyond the expected amplitude reduction due to a $\eta_s = 0.01$, we perform an additional numerical analysis on a flat plate with a comparable value of damping. The results [Figs. 8(c) and 8(d)] show that a much lower level of attenuation should be expected when the DZIM is not present. This comparison suggests that the DZIM produces also a significant amplification of the damping effect. These results are consistent with recent experimental studies [63,64] on locally resonant acoustic metamaterials that

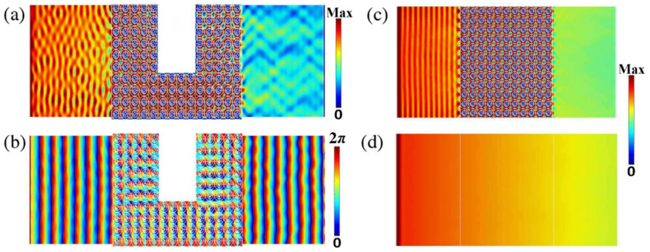

FIG. 8. Numerical simulations showing the effect of damping in a DZIM material. (a) and (b) show the phase and amplitude distributions of the wave field for the supercoupling case when a loss factor $\eta_s = 0.01$ is added to the whole structure. Comparisons of the amplitude attenuation level obtained in identical damped waveguides with (c) and without DZIM (d) are also presented. A significant amplification of the attenuation level can be observed clearly.

demonstrated how losses, even in a small amount, might have a strong impact on the dynamic response. Nevertheless, further theoretical analyses are required to rigorously assess this attenuation amplification mechanism in the presence of double-zero material properties.

Overall, the measurements confirm the theoretical and numerical predictions by clearly indicating that the A_0 mode can be propagated undistorted through the U-shaped DZIM waveguide channel. Nevertheless, significant amplitude attenuation takes place during the transmission, which is, in general, not due to backscattering but due to an enhanced effect of damping.

III. CONCLUSIONS

We present and experimentally demonstrate the design of a double-zero-index structural waveguide that is able to achieve simultaneous zero effective density and elastic compliance. The design leverages locally resonant geometric tapers that are used as fundamental unit cells to achieve and tune Dirac-like dispersion at the center of the Brillouin zone. We show both by theoretical and numerical methods that the material can be mapped to a double-zero effective medium when excited in the neighborhood of the Dirac-like point. Full-field numerical simulations show that this material can be used to achieve cloaking and supercoupling in elastic waveguides. Both theoretical and numerical results are confirmed by experimental measurements that validate the design and provide conclusive evidence that double-zero properties can be successfully achieved in solids. This study also highlights the important role of damping when locally resonant materials are excited in the proximity of zero effective density conditions. While the phase profile is not altered, the amplitude of the transmitted wave can suffer a severe reduction.

ACKNOWLEDGMENTS

The authors gratefully acknowledge the financial support of the Air Force Office of Scientific Research under Grant No. YIP FA9550-15-1-0133.

APPENDIX: SUPPLEMENTARY INFO

1. Details on numerical simulations and experimental setup

The full-wave simulations performed throughout the paper are obtained using a commercial finite-element solver (COMSOL MULTIPHYSICS). The thin plate is built out of aluminum with the following properties: Young's modulus $E = 70$ GPa, density $\rho = 2700\ \mathrm{kg/m^3}$, and Poisson's ratio $\nu = 0.33$. Perfectly matched layers are used on the outer boundaries to avoid reflections. For the experimental setup, additional details are provided below. The experimental sample is mounted in an aluminum frame providing clamped-free boundary conditions. A 3M viscoelastic tape (3M 2552 Damping Foil Tape) is used all around the panel to minimize the effect of boundary reflections. An array of nine MFC patches is surface bonded on the plate and simultaneously actuated to generate an A_0 (quasi-) planar incident wave. The actual plate used in the experimental setup is shown in Fig. 9(a). The main difference with the numerical model consists of extended edges of the U-shaped section (marked by the dashed areas) that are used to enforce the clamped boundaries. Numerical simulations [Fig. 9(b)] indicate that this modification of the boundary conditions does not alter the overall behavior of the DZIM channel with respect to the original all-clamped boundary.

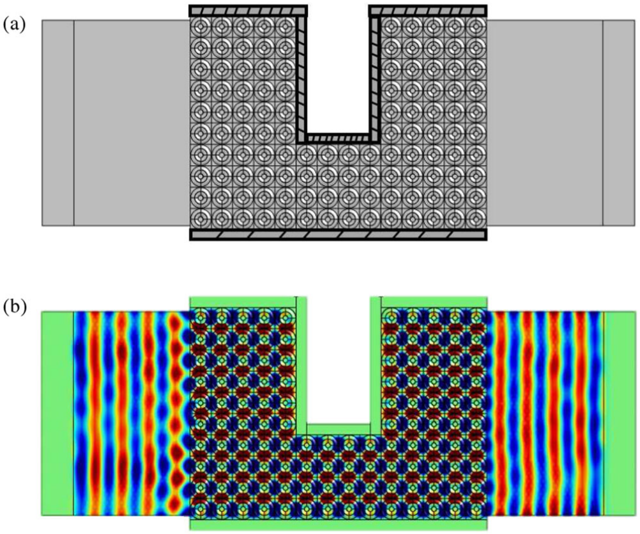

FIG. 9. (a) Schematic view of the experimental test bed. The edges of the DZIM slab (indicated by the dark dashed areas) are extended in order to allow for clamping. (b) Full-field numerical simulations show that the planar wave front of the transmitted wave is practically unaffected.

2. Details on the derivation of Eq. (6)

Below, we provide the detailed expression of the elements in Eq. (6) for our 3D bulk medium. Note that the spatial distribution of the material properties $\rho(\vec{r})$, $\lambda(\vec{r})$, and $\mu(\vec{r})$ is described by step functions. The gradient of these functions generates Dirac (δ) functions, i.e., $\boldsymbol{\nabla}\lambda(\vec{r}) = \lambda_0\delta(\vec{r} = \vec{r}_0)\vec{n}$, where $\vec{r}_0$ stands for the interface between the vacuum layer and the aluminum plate, and $\vec{n}$ is the normal to the interface pointing toward the aluminum domain. By substituting into Eq. (6), the x component of $\vec{p}_{jl}$ is

$$\begin{aligned}
p_{x_{jl}} = \Bigg\{ & \int_{\text{unit cell}} \Bigg[(\lambda_0+\mu_0)\left(\frac{\partial u_{j0}}{\partial x}+\frac{\partial v_{j0}}{\partial y}+\frac{\partial w_{j0}}{\partial z}\right)*u_{l0}^* \\
& +(\lambda_0+\mu_0)\left(\frac{\partial u_{j0}}{\partial x}*u_{l0}^*+\frac{\partial u_{j0}}{\partial y}*v_{l0}^*+\frac{\partial u_{j0}}{\partial z}*w_{l0}^*\right) \\
& +2\mu_0\left(\frac{\partial u_{j0}}{\partial x}*u_{l0}^*+\frac{\partial v_{j0}}{\partial x}*v_{l0}^*+\frac{\partial w_{j0}}{\partial x}*w_{l0}^*\right)\Bigg]dV \\
& +\oint_{\text{interface}}[\lambda_0 u_{j0}*(n_x u_{l0}^*+n_y v_{l0}^*+n_z w_{l0}^*) \\
& +\mu_0(n_y v_{j0}*u_{l0}^*+n_z w_{j0}*u_{l0}^*-n_x v_{j0}*v_{l0}^*-n_x w_{j0}*w_{l0}^*) \\
& +2\mu_0 n_x(u_{j0}*u_{l0}^*+v_{j0}*v_{l0}^*+w_{j0}*w_{l0}^*)]dA\Bigg\}\frac{(2\pi)^3}{V},
\end{aligned} \tag{A1}$$

while the y component is

$$\begin{aligned}
p_{y_{jl}} = \Bigg\{ & \int_{\text{unit cell}} \Bigg[(\lambda_0+\mu_0)\left(\frac{\partial u_{j0}}{\partial x}+\frac{\partial v_{j0}}{\partial y}+\frac{\partial w_{j0}}{\partial z}\right)*v_{l0}^* \\
& +(\lambda_0+\mu_0)\left(\frac{\partial v_{j0}}{\partial x}*u_{l0}^*+\frac{\partial v_{j0}}{\partial y}*v_{l0}^*+\frac{\partial v_{j0}}{\partial z}*w_{l0}^*\right) \\
& +2\mu_0\left(\frac{\partial u_{j0}}{\partial y}*u_{l0}^*+\frac{\partial v_{j0}}{\partial y}*v_{l0}^*+\frac{\partial w_{j0}}{\partial y}*w_{l0}^*\right)\Bigg]dV \\
& +\oint_{\text{interface}}[\lambda_0 v_{j0}*(n_x u_{l0}^*+n_y v_{l0}^*+n_z w_{l0}^*) \\
& +\mu_0(n_x u_{j0}*v_{l0}^*+n_z w_{j0}*v_{l0}^*-n_y u_{j0}*u_{l0}^*-n_y w_{j0}*w_{l0}^*) \\
& +2\mu_0 n_y(u_{j0}*u_{l0}^*+v_{j0}*v_{l0}^*+w_{j0}*w_{l0}^*)]dA\Bigg\}\frac{(2\pi)^3}{V}.
\end{aligned} \tag{A2}$$

The numerical values of the elements of $\vec{p}_{jl}$ can be obtained by performing numerical integrations based on the knowledge of the Bloch states.

3. Amplitude and phase distribution contours

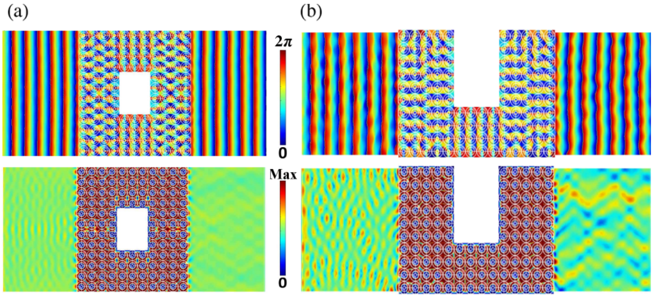

FIG. 10. Amplitude and phase distribution of the wave field for the (a) cloaking and (b) supercoupling effects illustrated in Fig. 6.

[1] R. V. Craster and S. Guenneau, *Acoustic Metamaterials: Negative Refraction, Imaging, Lensing and Cloaking* (Springer, Heidelberg, 2012).

[2] P. A. Deymier, *Acoustic Metamaterials and Phononic Crystals* (Springer, Heidelberg, 2013).

[3] V. G. Veselago, The electrodynamics of substances with simultaneously negative values of ϵ and μ, Sov. Phys. Usp. **10**, 509 (1968).

[4] J. B. Pendry, Negative Refraction Makes a Perfect Lens, Phys. Rev. Lett. **85**, 3966 (2000).

[5] D. R. Smith, W. J. Padilla, D. C. Vier, S. C. Nemat-Nasser, and S. Schultz, Composite Medium with Simultaneously Negative Permeability and Permittivity, Phys. Rev. Lett. **84**, 4184 (2000).

[6] D. R. Smith, Experimental verification of a negative index of refraction, Science **292**, 77 (2001).

[7] M. S. Kushwaha, P. Halevi, L. Dobrzynski, and B. Djafari-Rouhani, Acoustic Band Structure of Periodic Elastic Composites, Phys. Rev. Lett. **71**, 2022 (1993).

[8] F. R. Montero de Espinosa, E. Jiménez, and M. Torres, Ultrasonic Band Gap in a Periodic Two-Dimensional Composite, Phys. Rev. Lett. **80**, 1208 (1998).

[9] S. Yang, J. H. Page, Z. Liu, M. L. Cowan, C. T. Chan, and P. Sheng, Ultrasound Tunneling through 3*d* Phononic Crystals, Phys. Rev. Lett. **88**, 1043011 (2002).

[10] H. Sanchis-Alepuz, Y. A. Kosevich, and J. Sanchez-Dehesa, Acoustic Analogue of Electronic Bloch Oscillations and Resonant Zener Tunneling in Ultrasonic Superlattices, Phys. Rev. Lett. **98**, 134301 (2007).

[11] D. Garcia-Pablos, M. Sigalas, F. R. Montero de Espinosa, M. Torres, M. Kafesaki, and N. Garcia, Theory and Experiments on Elastic Band Gaps, Phys. Rev. Lett. **84**, 4349 (2000).

[12] J. O. Vasseur, P. A. Deymier, B. Chenni, B. Djafari-Rouhani, L. Dobrzynski, and D. Prevost, Experimental and Theoretical Evidence for the Existence of Absolute Acoustic Band Gaps in Two-Dimensional Solid Phononic Crystals, Phys. Rev. Lett. **86**, 3012 (2001).

[13] S. Zhang, L. Yin, and N. Fang, Focusing Ultrasound with an Acoustic Metamaterial Network, Phys. Rev. Lett. **102**, 194301 (2009).

[14] G. Lerosey, J. de Rosny, A. Tourin, and M. Fink, Focusing beyond the diffraction limit with far-field time reversal, Science **315**, 1120 (2007).

[15] R. Abasi, L. Markley, and G. V. Eleftheriades, Experimental verification of subwavelength acoustic focusing using a near-field array of closely spaced elements, J. Acoust. Soc. Am. **130**, EL405 (2011).

[16] Y. Li, B. Liang, X. Tao, X. Zhu, X. Zou, and J. Cheng, Acoustic focusing by coiling up space, Appl. Phys. Lett. **101**, 233508 (2012).

[17] H. Zhu and F. Semperlotti, Metamaterial based embedded acoustic filters for structural applications, AIP Adv. **3**, 092121 (2013).

[18] Z. He, Y. Heng, S. Peng, Y. Ding, M. Ke, and Z. Liu, Acoustic collimating beams by negative refraction in two-dimensional phononic crystal, J. Appl. Phys. **105**, 116105 (2009).

[19] O. A. Kaya, A. Cicek, and B. Ulug, Self-collimated slow sound in sonic crystals, J. Phys. D **45**, 365101 (2012).
[20] J. Mei, B. Hou, M. Ke, S. Peng, H. Jia, Z. Liu, J. Shi, W. Wen, and P. Sheng, Acoustic wave transmission through a bull's eye structure, Appl. Phys. Lett. **92**, 124106 (2008).
[21] J. J. Park, C. M. Park, K. J. B. Lee, and S. H. Lee, Acoustic superlens using membrane-based metamaterials, Appl. Phys. Lett. **106**, 051901 (2015).
[22] J. Christensen and F. J. Garca de Abajo, Acoustic field enhancement and subwavelength imaging by coupling to slab waveguide modes, Appl. Phys. Lett. **97**, 164103 (2010).
[23] J. Li, L. Fok, X. Yin, G. Bartal, and X. Zhang, Experimental demonstration of an acoustic magnifying hyperlens, Nat. Mater. **8**, 931 (2009).
[24] F. Semperlotti and H. Zhu, Achieving selective damage interrogation and sub-wavelength resolution in thin plates with embedded metamaterial acoustic lenses, J. Appl. Phys. **116**, 054906 (2014).
[25] M. Ambati, N. Fang, C. Sun, and X. Zhang, Surface resonant states and superlensing in acoustic metamaterials, Phys. Rev. B **75**, 195447 (2007).
[26] C. M. Park, J. J. Park, S. H. Lee, Y. M. Seo, C. K. Kim, and S. H. Lee, Amplification of Acoustic Evanescent Waves Using Metamaterial Slabs, Phys. Rev. Lett. **107**, 194301 (2011).
[27] B. Morvan, A. Tinel, A.-C. Hladky-Hennion, J. Vasseur, and B. Dubus, Experimental demonstration of the negative refraction of a transverse elastic wave in a two-dimensional solid phononic crystal, Appl. Phys. Lett. **96**, 101905 (2010).
[28] J. Pierre, O. Boyko, L. Belliard, J. O. Vasseur, and B. Bonello, Negative refraction of zero order flexural Lamb waves through a two-dimensional phononic crystal, Appl. Phys. Lett. **97**, 121919 (2010).
[29] N. Kaina, F. Lemoult, M. Fink, and G. Lerosey, Negative refractive index and acoustic superlens from multiple scattering in single negative metamaterials, Nature (London) **525**, 77 (2015).
[30] V. M. García-Chocano, J. Christensen, and José Sánchez-Dehesa, Negative Refraction and Energy Funneling by Hyperbolic Materials: An Experimental Demonstration in Acoustics, Phys. Rev. Lett. **112**, 144301 (2014).
[31] A. Alù, M. G. Silveirinha, A. Salandrino, and N. Engheta, Epsilon-near-zero metamaterials and electromagnetic sources: Tailoring the radiation phase pattern, Phys. Rev. B **75**, 155410 (2007).
[32] S. N. Enoch, G. Tayeb, P. Sabouroux, N. Guérin, and P. Vincent, A Metamaterial for Directive Emission, Phys. Rev. Lett. **89**, 213902 (2002).
[33] A. Alu, F. Bilotti, N. Engheta, and L. Vegni, Metamaterial covers over a small aperture, IEEE Trans. Antennas Propag. **54**, 1632 (2006).
[34] J. C. Soric, N. Engheta, S. Maci, and A. Alu, Omnidirectional metamaterial antennas based on ε-near-zero channel matching, IEEE Trans. Antennas Propag. **61**, 33 (2013).
[35] R. W. Ziolkowski, Propagation in and scattering from a matched metamaterial having a zero index of refraction, Phys. Rev. E **70**, 046608 (2004).
[36] M. Silveirinha and N. Engheta, Tunneling of Electromagnetic Energy through Subwavelength Channels and Bends Using ε-Near-Zero Materials, Phys. Rev. Lett. **97**, 157403 (2006).
[37] M. Silveirinha and N. Engheta, Design of matched zero-index metamaterials using nonmagnetic inclusions in epsilon-near-zero media, Phys. Rev. B **75**, 075119 (2007).
[38] D. C. Adams, S. Inampudi, T. Ribaudo, D. Slocum, S. Vangala, N. A. Kuhta, W. D. Goodhue, V. A. Podolskiy, and D. Wasserman, Funneling Light through a Subwavelength Aperture with Epsilon-Near-Zero Materials, Phys. Rev. Lett. **107**, 133901 (2011).
[39] Mario G. Silveirinha and N. Engheta, Transporting an Image through a Subwavelength Hole, Phys. Rev. Lett. **102**, 103902 (2009).
[40] G. V. Naik, J. Kim, and A. Boltasseva, Oxides and nitrides as alternative plasmonic materials in the optical range, Opt. Mater. Express **1**, 1090 (2011).
[41] R. Fleury and A. Alù, Extraordinary Sound Transmission through Density-Near-Zero Ultranarrow Channels, Phys. Rev. Lett. **111**, 055501 (2013).
[42] L. Zheng, Y. Wu, X. Ni, Z. Chen, M. Lu, and Y. Chen, Acoustic cloaking by a near-zero-index phononic crystal, Appl. Phys. Lett. **104**, 161904 (2014).
[43] X. Xu, P. Li, X. Zhou, and G. Hu, Experimental study on acoustic subwavelength imaging based on zero-mass metamaterials, Europhys. Lett. **109**, 28001 (2015).
[44] F. Liu, Y. Lai, X. Huang, and C. T. Chan, Dirac cones at $k = 0$ in phononic crystals, Phys. Rev. B **84**, 224113 (2011).
[45] T. C. Wu, Y. Lai, Z. H. Hang, H. Zheng, and C. T. Chan, Dirac cones induced by accidental degeneracy in photonic crystals and zero-refractive-index materials, Nat. Mater. **10**, 582 (2011).
[46] F. Liu, X. Huang, and C. T. Chan, Dirac cones at $k = 0$ in acoustic crystals and zero refractive index acoustic materials, Appl. Phys. Lett. **100**, 071911 (2012).
[47] Y. Li, S. Kita, P. Muoz, O. Reshef, D. I. Vulis, M. Yin, M. Lonar, and E. Mazur, Realization of an all-dielectric zero-index optical metamaterial, Nat. Photonics **7**, 791 (2013).
[48] P. Moitra, Y. Yang, Z. Anderson, I. I. Kravchenko, D. P. Briggs, and J. Valentine, On-chip zero-index metamaterials, Nat. Photonics **9**, 738 (2015).
[49] S. Wu and J. Mei, Flat band degeneracy and near-zero refractive index materials in acoustic crystals, AIP Adv. **6**, 015204 (2016).
[50] M. W. Ashraf and M. Faryad, On the mapping of Dirac-like cone dispersion in dielectric photonic crystals to an effective zero-index medium, J. Opt. Soc. Am. B **33**, 1008 (2016).
[51] F. Liu, F. Zhang, W. Wei, N. Hu, G. Deng, and Z. Wang, Scattering of waves by three-dimensional obstacles in elastic metamaterials with zero index, Phys. Rev. B **94**, 224102 (2016).
[52] H. Zhu and F. Semperlotti, Phononic thin plates with embedded acoustic black holes, Phys. Rev. B **91**, 104304 (2015).
[53] H. Zhu and F. Semperlotti, Anomalous Refraction of Acoustic Guided Waves in Solids with Geometrically Tapered Metasurfaces, Phys. Rev. Lett. **117**, 034302 (2016).
[54] H. Zhu and F. Semperlotti, Two-dimensional structure-embedded acoustic lenses based on periodic acoustic black holes, arXiv:1701.03445.

[55] J. Mei, Y. Wu, C. T. Chan, and Z. Q. Zhang, First-principles study of Dirac and Dirac-like cones in phononic and photonic crystals, Phys. Rev. B **86**, 035141 (2012).

[56] M. Willatzen and Lok C. Lew Yan Voon, *The k·p Method: Electronic Properties of Semiconductors* (Springer, New York, 2009).

[57] Z. Hou and B. M. Assouar, Modeling of Lamb wave propagation in plate with two-dimensional phononic crystal layer coated on uniform substrate using plane-wave-expansion method, Phys. Lett. A **372**, 2091 (2008).

[58] Y. Lai, Y. Wu, P. Sheng, and Z. Zhang, Hybrid elastic solids, Nat. Mater. **10**, 620 (2011).

[59] R. V. Craster, J. Kaplunov, and A. V. Pichugin, High-frequency homogenization for periodic media, Proc. R. Soc. A **466**, 2341 (2010).

[60] R. V. Craster, J. Kaplunov, E. Nolde, and S. Guenneau, High-frequency homogenization for checkerboard structures: Defect modes, ultrarefraction, and all-angle negative refraction, J. Opt. Soc. Am. A **28**, 1032 (2011).

[61] Y. Ding, Z. Liu, C. Qiu, and J. Shi, Metamaterial with Simultaneously Negative Bulk Modulus and Mass Density, Phys. Rev. Lett. **99**, 093904 (2007).

[62] Y. Wu, Y. Lai, and Z. Zhang, Effective medium theory for elastic metamaterials in two dimensions, Phys. Rev. B **76**, 205313 (2007).

[63] M. Molern, M. Serra-Garcia, and C. Daraio, Visco-thermal effects in acoustic metamaterials: From total transmission to total reflection and high absorption, New J. Phys. **18**, 033003 (2016).

[64] V. C. Henríquez, V. M. García-Chocano, and J. Sánchez-Dehesa, Viscothermal Losses in Double-Negative Acoustic Metamaterials, Phys. Rev. Applied **8**, 014029 (2017).